

Cite this: *Chem. Sci.*, 2025, **16**, 19192

All publication charges for this article have been paid for by the Royal Society of Chemistry

## Structure–property relationships of responsive doubly-threaded slide-ring polycatenane networks

Guancen Liu, <sup>a</sup> Jongwon Oh, <sup>a,b</sup> Yuan Tian, <sup>a,b,c</sup> Jerald E. Hertzog, <sup>b</sup> Heyi Liang, <sup>b</sup> Benjamin W. Rawe, <sup>b</sup> Natsumi Nitta, <sup>b</sup> Charlie A. Lindberg, <sup>b</sup> Hojin Kim, <sup>bd</sup> Juan J. de Pablo<sup>\*bcef</sup> and Stuart J. Rowan <sup>\*abg</sup>

Slide-ring polycatenane networks (SR-PCNs) are covalent polymer networks that contain interlocked doubly threaded rings that serve as additional topological constraints. These rings are catenated by the covalent polymer network, enabling them to slide along the polymer backbone between the covalent crosslinks. Herein, the SR-PCN synthesis is achieved by reacting a metal-templated doubly threaded pseudo[3]rotaxane (P3R) crosslinker with a chain extender and a covalent crosslinking moiety. The focus of this work is to explore the impact that monomer structure has on the SR-PCN synthesis, with the goal of increasing the reaction kinetics of the P3R to optimize ring incorporation in the network and minimize side reactions. It is shown that through monomer optimization it is possible to synthesize SR-PCNs with high gel fractions and ring content, allowing a detailed evaluation of the influence of the rings on the properties of these interlocked networks. Compared with control covalent networks and a tangled network, formed using a 1:2 metal–ligand complex, SR-PCNs exhibit enhanced swelling and frequency-dependent viscoelastic behavior, which are attributed to the motion of the rings. Molecular simulations of model interlocked networks elucidate the underlying mechanisms governing the mechanical behavior and provide insights into the structural changes induced by the rings. In addition, the responsive behavior of these SR-PCNs is explored upon exposure to stimuli that impact the ring mobility, such as changes in solvent, metalation, and protonation of the ligand moieties.

Received 21st July 2025  
Accepted 10th September 2025  
DOI: 10.1039/d5sc05459a  
[rsc.li/chemical-science](http://rsc.li/chemical-science)

## Introduction

Mechanically interlocked molecules (MIMs) are a class of molecules characterized by the presence of the mechanical bond.<sup>1–6</sup> The most prevalent types of MIMs are catenanes, which are interlocked macrocycles (rings), and rotaxanes, which consist of a ring threaded onto a dumbbell component.<sup>7–9</sup> The presence of mechanical bonds, as opposed to covalent bonds, between components generally enhances the conformational freedom of the interlocked components, enabling access to distinct motions such as rotation, elongation, twisting, and

sliding relative to their interlocked partner.<sup>10–12</sup> Incorporating MIMs into polymeric materials allows access to mechanically interlocked polymers (MIPs).<sup>13–15</sup> Among the family of MIPs, slide-ring networks (SRN, a subclass of polyrotaxanes) have been demonstrated to exhibit remarkable physicochemical and mechanical properties as a result of the mobility of the rings along the polymer backbone.<sup>16,17</sup> This mobility leads to enhanced toughness,<sup>18,19</sup> increased extensibility,<sup>20–23</sup> stimuli-responsive actuation,<sup>24</sup> shape memory,<sup>25</sup> stress relaxation,<sup>12</sup> and rapid energy dissipation.<sup>26</sup> Typical synthetic approaches to SRNs involve crosslinking the rings on a polyrotaxane to form figure-of-eight crosslinks (Fig. 1a),<sup>17,18,21,27</sup> or using a polymer to crosslink the rings.<sup>19,22,23,28,29</sup> Most SRNs reported to date are singly-threaded (one polymer chain threaded through a ring). It is possible to access more complex interlocked structures, such as doubly-threaded (dt) MIMs, where two dumbbell components are threaded through one ring, in high yield,<sup>30–33</sup> which has subsequently led to a few reports of dtMIPs.<sup>34–38</sup> A related class of MIPs is polycatenanes, where the mechanical bond is the result of interlocked rings (*i.e.*, a catenane moiety).<sup>39–41</sup> To date, the majority of polycatenane networks have focused on systems that have a singly-threaded [2]catenane as their interlocked component.<sup>42–49</sup>

<sup>a</sup>Department of Chemistry, University of Chicago, Chicago, IL 60637, USA. E-mail: [stuartrowan@uchicago.edu](mailto:stuartrowan@uchicago.edu)

<sup>b</sup>Pritzker School of Molecular Engineering, University of Chicago, Chicago, IL 60637, USA. E-mail: [jjd8110@nyu.edu](mailto:jjd8110@nyu.edu)

<sup>c</sup>Department of Chemical and Biomolecular Engineering, Tandon School of Engineering, New York University, Brooklyn, NY 11201, USA

<sup>d</sup>James Franck Institute, University of Chicago, Chicago, IL 60637, USA

<sup>e</sup>Department of Computer Science, Courant Institute of Mathematical Sciences, New York University, New York, NY 10012, USA

<sup>f</sup>Department of Physics, New York University, New York, NY 10003, USA

<sup>g</sup>Chemical Science and Engineering Division and Center for Molecular Engineering, Argonne National Laboratory, 9700 S. Cass Ave., Lemont, IL 60434, USA

† These authors contributed equally to this work.



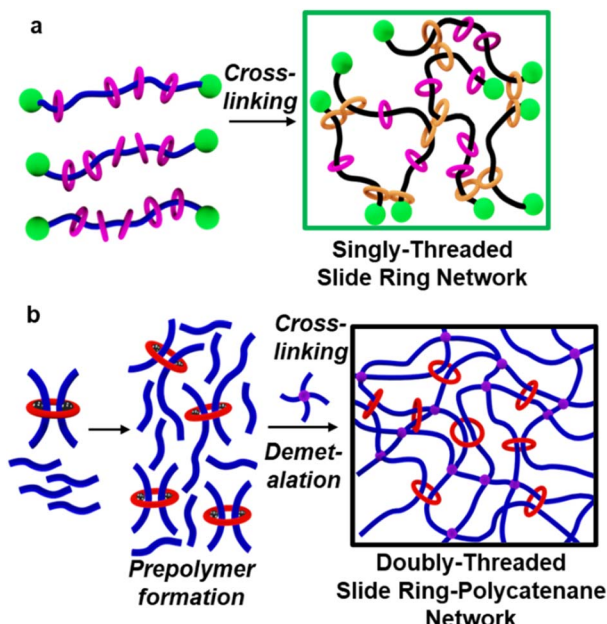


Fig. 1 (a) Synthesis of singly-threaded slide-ring networks (SRN) by chemically crosslinking the rings of a polyrotaxane, resulting in figure-of-eight crosslinks. (b) Synthesis of slide-ring polycatenane network (SR-PCN) using a metal ion templated doubly-threaded pseudo[3]rotaxane (P3R) to react with an excess of chain extender followed by reaction with a covalent crosslink. After crosslinking, the metal ion is removed to yield the SR-PCN.

Networks with multiply-threaded catenane moieties include Olympic gels and kinetoplast DNAs.<sup>48,50–56</sup> A subclass of multiply-threaded catenane-containing networks are the slide-ring polycatenane networks (SR-PCN, Fig. 1b). These SR-PCNs contain crosslinking doubly-threaded (dt) rings embedded within a percolating covalent network.<sup>57</sup> The synthetic route to such networks employed a dt-pseudo[3]rotaxane (P3R) **1:2<sub>2</sub>:Zn(II)<sub>2</sub>** (Fig. 2, *a* = 0–30 mol%) crosslinker, formed from the self-assembly of a ditopic 2,6-bis(*N*-alkyl-benzimidazolyl)pyridine (BIP) ring<sup>58</sup> **1** and two alkyne endcapped linear BIP-containing threads **2** with a transition metal ion, Zn(II).<sup>59,60</sup> **1:2<sub>2</sub>:Zn(II)<sub>2</sub>** was polymerized *via* a catalyst-free nitrile-oxide/alkyne cycloaddition in the presence of a covalent tetra-alkyne poly(ethylene glycol) (PEG) crosslinker **4<sub>5k</sub>** ( $M_n = 5 \text{ kg mol}^{-1}$ ) (Fig. 2, *b* = 100–*a* mol%) and a *bis*-nitrile oxide chain extender **3a** (Fig. 2). After curing, the networks were washed to remove the sol fraction, yielding the metalated gel **5<sub>a/bM</sub>**. The demetalated gel **5<sub>a/bD</sub>** (Fig. 2, M corresponds to metalated gel, and D corresponds to demetalated networks) was accessed using tetra-butylammonium hydroxide (TBAOH). Studies showed that *ca.* 30% of the macrocycle was retained within the network after demetalation and washing. Furthermore, the gel fraction (GF, wt%) of **5<sub>a/bD</sub>** dropped significantly when introducing more of the P3R crosslink in the synthesis. Taken together, these results suggest that the P3R crosslinker was not incorporated into the network as efficiently as the covalent crosslinker **4<sub>5k</sub>**, which limited the ability to carry out detailed mechanical studies to evaluate the impact of the ring on the properties of

these new networks. Thus, with the goal of gaining a better understanding of the properties of this class of MIP networks and how the incorporation of the mobile ring impacts their properties, the work herein is focused on (1) improving the synthesis of the SR-PCN by redesigning the system to allow for a more efficient incorporation of the P3R into the network, (2) preparing a series of control networks, (3) carrying out studies on their mechanical properties, and (4) interpreting the experimental studies through detailed simulations of molecular models of the materials.

## Results and discussion

It was hypothesized that the limited incorporation of the P3R (**1:2<sub>2</sub>:Zn(II)<sub>2</sub>**) in the prior SR-PCN studies was a result of the slower reaction kinetics of the *bis*-nitrile oxide **3a** reacting with **1:2<sub>2</sub>:Zn(II)<sub>2</sub>** (Fig. S1–S8) relative to the *tetra*-PEG alkyne **4<sub>5k</sub>**. Thus, initial investigations focused on understanding the reactivity of the different components. As such, **1:2<sub>2</sub>:Zn(II)<sub>2</sub>** and **4<sub>5k</sub>** were reacted with excess **3a** (20 equiv.) and monitored *via* proton nuclear magnetic resonance (<sup>1</sup>H-NMR) spectroscopy (Fig. S9 and S10). While **4<sub>5k</sub>** took 15 h to fully react ( $k = 1.2 \times 10^{-3} \text{ M}^{-1} \text{ s}^{-1}$ ), **1:2<sub>2</sub>:Zn(II)<sub>2</sub>** required much longer (>54 h) for the reaction to go to completion ( $k = 2.9 \times 10^{-4} \text{ M}^{-1} \text{ s}^{-1}$ ) (Fig. 3a). In addition, while the reaction with **4<sub>5k</sub>** shows only one signal in the isoxazole proton ( $H_{\text{isox}}$ ) region (*ca.* 5.96 ppm) (Fig. S9), the reaction with **1:2<sub>2</sub>:Zn(II)<sub>2</sub>** showed the presence of two peaks with a second peak (*ca.* 6.06 ppm, 35% of the total  $H_{\text{isox}}$  by <sup>1</sup>H-NMR spectroscopy) that is shifted downfield relative to the major signal (*ca.* 5.96 ppm) (Fig. 3b and S10). In a separate reaction using **1:2<sub>2</sub>:Zn(II)<sub>2</sub>** and **3a** (2 equiv.), this downfield-shifted signal becomes the predominant signal (66% of the total  $H_{\text{isox}}$ ) (Fig. S11). This suggests that the downfield signal comes from the cyclization of one of the threads in **1:2<sub>2</sub>:Zn(II)<sub>2</sub>** with **3a** to form a catenane. In fact, after demetalation of this reaction mixture, <sup>1</sup>H-NMR shows the presence of upfield-shifted signals corresponding to the pyridyl protons consistent with interlocked BIP-based compounds<sup>39–41,59–62</sup> (Fig. S12) and matrix-assisted laser desorption/ionization-time of flight (MALDI-TOF) mass spectrometry confirmed the presence of [2] and [3] catenated species (Fig. S13). Taken together, these results not only show that **1:2<sub>2</sub>:Zn(II)<sub>2</sub>** reacts with **3a** more slowly than **4<sub>5k</sub>**, but also that it can form catenated byproducts that hinder network formation.

To limit the catenane side reaction, the *bis*-nitrile oxide **3b** was synthesized with a longer hexaethylene glycol core (Fig. 2 and S14–S16). When reacting **3b** (20 equiv.) with **1:2<sub>2</sub>:Zn(II)<sub>2</sub>**, the downfield shifted signal in the isoxazole proton decreased to *ca.* 18% of the total  $H_{\text{isox}}$  (Fig. 3b and S17–S20), indicating less catenane formation with the longer chain. However, the reaction rate did not change significantly. Hypothesizing that steric considerations are the reason for the relatively slow reaction rate of **1:2<sub>2</sub>:Zn(II)<sub>2</sub>** with **3a/3b**, it was decided to access P3Rs with BIP thread components **6a–c** that have oligoethylene glycol extensions (*n* = 3, 6, or 9, respectively) between the ligand and alkyne (Fig. 2 and S21–S29). With these components in hand, a series of dtP3Rs with macrocycle **1** and the different threads

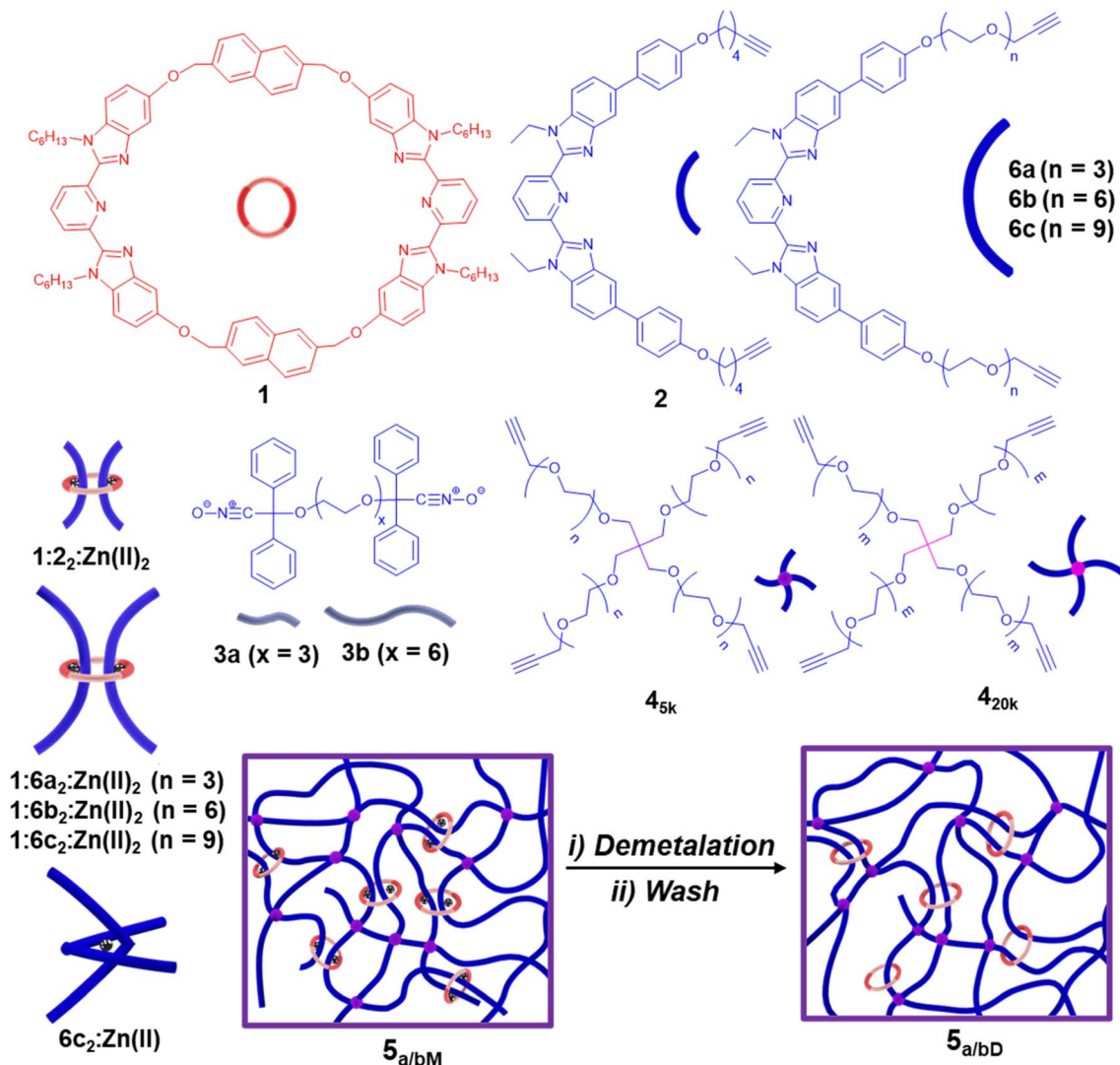


**Fig. 2** Structure of the components used in the synthesis of SR-PCN via nitrile-oxide/alkyne cycloaddition polymerization – the doubly-threaded pseudo[3]rotaxanes (P3Rs)  $1:2_2:\text{Zn(II)}_2$  and  $1:6a_2:\text{Zn(II)}_2$ , covalent tetra-alkyne PEG crosslinks  $4_{5k}$  and  $4_{20k}$  ( $M_n = 5 \text{ kg mol}^{-1}$  and  $20 \text{ kg mol}^{-1}$ , respectively), 4-arm tetra-alkyne  $6c_2:\text{Zn(II)}_2$  formed by metal-ligand assembly, and bis-nitrile-oxide chain extenders  $3a$  and  $3b$ . Copolymerization of  $1:2_2:\text{Zn(II)}_2$  and  $4_{5k}$  with  $3a$  yielded a series of SR-PCNs  $5_{a/bM}$  by varying the ratio of P3R and covalent crosslink, and upon base treatment the demetalated  $5_{a/bD}$ .

**6a–c** were self-assembled with  $\text{Zn(II)}$  ions (Fig. 2 and S30–S38). Diffusion ordered spectroscopy (DOSY) confirmed the formation of larger P3R assemblies with the longer threads (Fig. S39–S48 and Table S1). The reaction of **3b** (20 equiv.) with  $1:6a_2:\text{Zn(II)}_2$  resulted in faster reaction kinetics relative to  $1:2_2:\text{Zn(II)}_2$  ( $k = 7.9 \times 10^{-4} \text{ M}^{-1} \text{ s}^{-1}$ ) (Fig. S49). The intensity of the downfield shifted byproduct signals (*ca.* 6.28–6.22 ppm) was also reduced to 15% of the major signal at *ca.* 6.20 ppm. Increasing the length of the spacer further revealed an additional enhancement in reaction kinetics. Reacting  $1:6b_2:\text{Zn(II)}_2$  or  $1:6c_2:\text{Zn(II)}_2$  with **3b** (20 equivs.) resulted in the reactions going to completion in *ca.* 15 h ( $k = 1.2 \times 10^{-3} \text{ M}^{-1} \text{ s}^{-1}$ ) (Fig. S50 and S51). Furthermore,  $^1\text{H-NMR}$  spectroscopy showed that the catenane byproduct signal was further reduced to 7% for  $1:6b_2:\text{Zn(II)}_2$  and 5% for  $1:6c_2:\text{Zn(II)}_2$  relative to the major signal (at *ca.* 6.20 ppm) (Fig. S50–S54). A summary of the

reaction times and the percent of catenane formed when reacting the different P3Rs with **3b** is summarized in Fig. S55 and S56.

Based on these studies, the synthesis of SR-PCNs was explored using **3b** and  $1:6c_2:\text{Zn(II)}_2$  (Fig. 4a). The P3R crosslinker  $1:6c_2:\text{Zn(II)}_2$  (20 mol%) was reacted with an excess of **3b** (200 mol%) before adding  $4_{5k}$  (80 mol%) to yield the SR-PCN  $7_{80/20M}$  (Fig. 4a and S57, see SI for details). After demetalation and washing, the gel fraction (GF) of  $7_{80/20D}$  was higher than that observed for  $5_{80/20D}$  (*ca.* 96% *vs.* *ca.* 83%).<sup>57</sup> To calculate the amount of macrocycles retained in the  $7_{80/20D}$  film,  $^1\text{H-NMR}$  analysis of the soluble fractions obtained from the washing and demetalation steps was carried out to determine how much macrocycles could be extracted from the film (eqn (S4), see SI for details). The data shows that *ca.* 19% of the macrocycle added to the reaction mixture was extracted from the  $7_{80/20D}$  film,

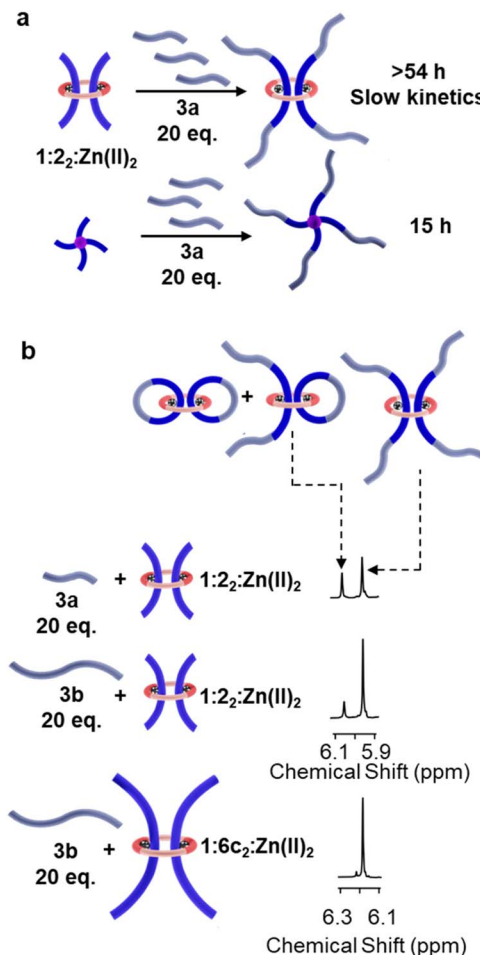


Fig. 3 Study of the reaction between different crosslinks and the chain extenders. (a) Schematics of reaction of  $1:2\text{-Zn(II)}_2$  and  $4_{5k}$  reacting with  $3\text{a}$ . (b) Region of the  $^1\text{H}$  NMR spectra (500 MHz, 5%  $\text{CD}_3\text{CN}$  in  $\text{CDCl}_3$ , 298 K) corresponding to the  $\text{H}_{\text{isox}}$  protons for  $1:2\text{-Zn(II)}_2$  reacting with  $3\text{a}$  and  $3\text{b}$ , as well as  $1:6\text{c}_2\text{-Zn(II)}_2$  reacting with  $3\text{b}$ . Chain extenders are shown in light blue for clarity.

suggesting that the amount of ring retained in the network is over 80% (see SI for details), significantly higher than had been previously reported (29%).<sup>57</sup> The swelling ratio ( $Q$ , vol%, see SI for details) of  $7_{80/20D}$  is 1100 vol% in *N*-methyl-2-pyrrolidone (NMP), and the resulting gels are relatively weak/brittle (Fig. 4b). To access tougher materials, a higher molecular weight PEG crosslinker  $4_{20k}$  (Fig. 2) ( $M_n = 20 \text{ kg mol}^{-1}$ ) was reacted with  $3\text{b}$  and  $1:6\text{c}_2\text{-Zn(II)}_2$  (20 mol%) to synthesize SR-PCN  $8_{80/20D}$  (Fig. 4a, S58 and S59, see SI for details). It was found that the swollen  $8_{80/20D}$  (970 vol% in NMP) is a much tougher material relative to  $7_{80/20D}$ , exhibiting a significantly larger stress-at-break (110 kPa for  $8_{80/20D}$  vs. 3 kPa for  $7_{80/20D}$ ) and strain-at-break (220% for  $8_{80/20D}$  vs. 60% for  $7_{80/20D}$ ) in tensile tests (Fig. 4b).

Having optimized the reaction components to access the SR-PCNs, the next step was to synthesize SR-PCNs with varying amounts of the P3R crosslinker. To that end, different ratios of the covalent crosslinker ( $4_{20k}$  from 90 mol% to 60 mol%) and

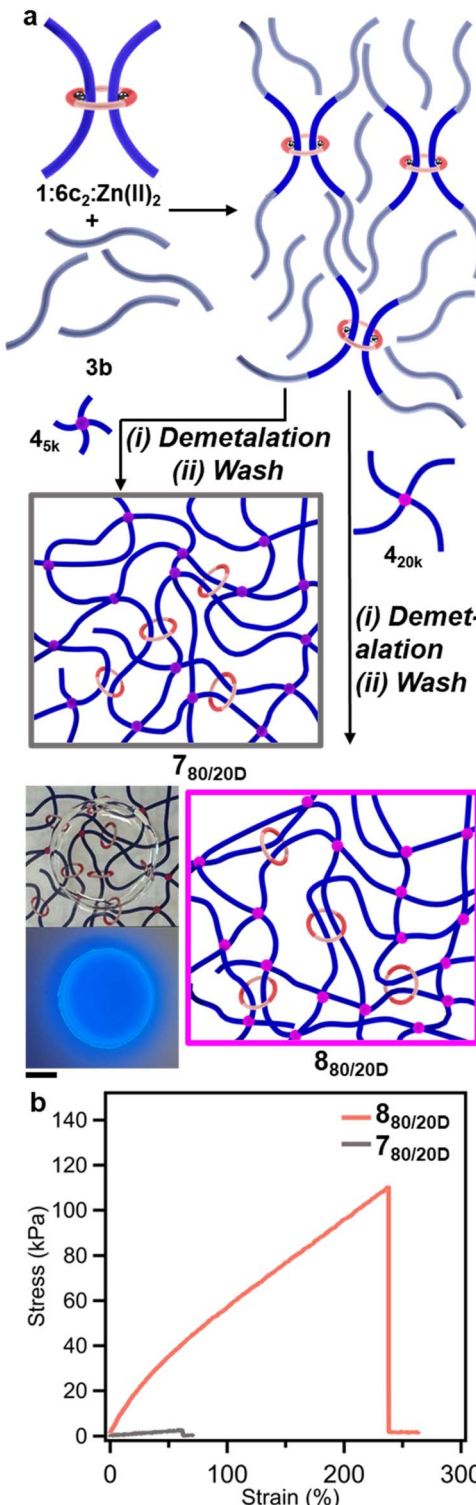


Fig. 4 (a) Schemes showing the synthesis of SR-PCNs  $7_{80/20D}$  and  $8_{80/20D}$  using P3R  $1:6\text{c}_2\text{-Zn(II)}_2$  to react with excess  $3\text{b}$  followed by addition of the crosslink  $4_{5k}$  or  $4_{20k}$ , respectively. Demetalation results in an optically clear film that fluoresces blue under 365 nm UV light, on the account of the free ligand.  $8_{80/20D}$  pictured, 1 cm scale bar. (b) Stress-strain curves of swollen  $7_{80/20D}$  and  $8_{80/20D}$  in *N*-methyl-2-pyrrolidone (NMP) with a strain rate of  $5 \text{ mm min}^{-1}$ .



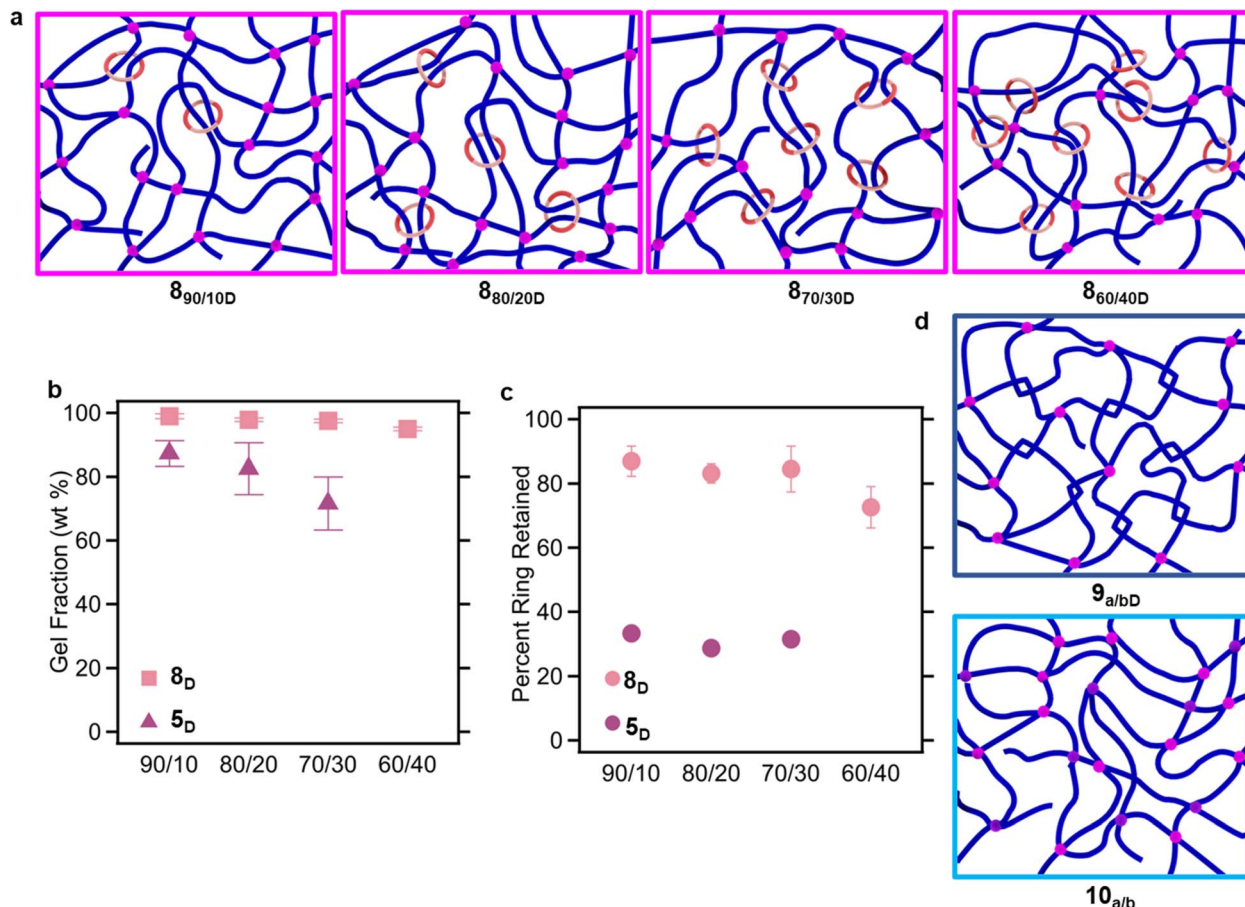


Fig. 5 (a) Schematic of SR-PCN  $8_{a/bD}$  with increasing number of rings ( $b = 10\text{--}40\text{ mol\%}$ ). (b) Comparison of the gel fraction (GF) of the synthesized SR-PCNs  $8_{a/bD}$  and  $5_{a/bD}$ . Data on  $5_{a/bD}$  from prior work.<sup>57</sup> (c) Percent of ring retained in the network  $8_{a/bD}$ , relative to that of networks  $5_{a/bD}$  (error bars omitted for clarity). Data of  $5_{a/bD}$  from prior work.<sup>57</sup> (d) Schematic of the two control networks  $9_{a/bM}$  and  $10_{a/b}$  synthesized from **3b** with different ratios of the crosslinkers  $4_{20k}$  and  $6c_2:\text{Zn(II)}$  or  $4_{5k}$ , respectively.  $9_{a/bM}$  was treated with TBAOH to yield  $9_{a/bD}$ .

the P3R crosslinker (**1:6c<sub>2</sub>:Zn(II)**) from 10 mol% to 40 mol% were reacted with **3b** to yield a series of SR-PCNs ( $8_{a/bM}$ ), where  $a$  and  $b$  are the relative mole percents of  $4_{20k}$  and **1:6c<sub>2</sub>:Zn(II)** used in the network synthesis, respectively (Table S2, see SI for details). After extensive washing with chloroform,  $8_{a/bM}$  films exhibited high GFs (>97%, Fig. S60) and after demetalation, the resulting  $8_{a/bD}$  (Fig. 5a) retained their high GFs (>95%, Fig. 5b). The amounts of macrocycle and thread in the soluble fractions were quantified by <sup>1</sup>H-NMR (Fig. S61, S62, and Table S3, see SI for details), allowing for determination of the amount of rings retained in the  $8_{a/bD}$  films to be >80% for  $b = 10\text{--}30\text{ mol\%}$  and ca. 73% for  $b = 40\text{ mol\%}$  (Fig. 5c).

To better understand the impact of the slide-ring (SR) in the SR-PCN, two control networks were synthesized. A series of BIP-containing networks formed with metallosupramolecular crosslinking units (Fig. 2 and S63–S66) were synthesized *via* the copolymerization of **3b** with varying ratios of  $4_{20k}$  and the tetra-alkyne **6c<sub>2</sub>:Zn(II)**, formed by self-assembly of two **6c** with zinc bis triflimide ( $\text{Zn(NTf}_2\text{)}_2$ ). The resulting networks  $9_{a/bM}$  ( $a$  and  $b$  are the mole percentage of  $4_{20k}$  and **6c<sub>2</sub>:Zn(II)** respectively) were washed and demetalated (Fig. S67–S69, and Table S4, see SI for details). These gels are termed here tangled networks  $9_{a/bD}$ .

(Fig. 5d), as the supramolecular crosslink has the potential to yield additional “trapped” chain entanglements, as has been shown by Zhukhovitskiy and coworkers.<sup>63,64</sup> The amount of thread in the soluble fraction of  $9_{a/bD}$  was quantified by <sup>1</sup>H-NMR (Table S3, see SI for details) and showed that >94% of the BIP moieties are retained in the  $9_{a/bD}$  films. A second set of control networks is the fully covalent networks  $10_{a/b}$ , which were synthesized by copolymerizing varying ratios of  $4_{20k}$  and  $4_{5k}$  (where  $a$  and  $b$  are the mole percentages of  $4_{20k}$  and  $4_{5k}$  crosslinkers, respectively) with **3b** (Fig. 5d, S70 and S71, see SI for details).  $4_{5k}$  was used as the control replacement for **1:6c<sub>2</sub>:Zn(II)** on account of their similar molecular weight. Both  $9_{a/bD}$  and  $10_{a/b}$  showed similarly high GF to  $8_{a/bD}$  (Fig. S72 and S73). A summary of all network compositions and their naming scheme is shown in Table 1.

With the three different classes of networks (**8–10**) in hand, the next step was to explore how the networks with dtsr crosslinks ( $8_{a/bD}$ ) compared to the control networks ( $9_{a/bD}$  and  $10_{a/b}$ ). As such,  $8_{a/bD}$ ,  $9_{a/bD}$ , and  $10_{a/b}$  were swollen in NMP. The swelling ratio,  $Q$ , of all the SR-PCNs is higher than that of the corresponding  $9_{a/bD}$  and  $10_{a/b}$  gels (Fig. S74 and S75). For example, the  $Q$  of  $8_{80/20D}$  (ca. 970%, Fig. 6a) is higher relative to

**Table 1** Component composition used in the synthesis of the networks

Network <sup>a</sup>	Component <i>a</i> (mol%)	Component <i>b</i> (mol%)
SR-PCN 7 <sub>a/bD</sub>	4 <sub>5k</sub> (80 mol%)	1:6c <sub>2</sub> :Zn(n) <sub>2</sub> (20 mol%)
SR-PCN 8 <sub>a/bD</sub>	4 <sub>20k</sub> (90–60 mol%)	1:6c <sub>2</sub> :Zn(n) <sub>2</sub> (10–40 mol%)
Tangled 9 <sub>a/bD</sub>	4 <sub>20k</sub> (90–60 mol%)	6c <sub>2</sub> :Zn(n) (10–40 mol%)
Covalent 10 <sub>a/b</sub>	4 <sub>20k</sub> (100–60 mol%)	4 <sub>5k</sub> (0–40 mol%)

<sup>a</sup> M corresponds to metalated gels and D corresponds to demetalated gels.

9<sub>80/20D</sub> (ca. 870%) and 10<sub>80/20</sub> (ca. 740%). This is consistent with the mobility of the SR crosslinks in 8<sub>a/bD</sub>, allowing greater swelling, as has been shown in other SRN architectures.<sup>17,61</sup> Small-amplitude oscillatory compression (SAOC) experiments were conducted to study the frequency-dependent viscoelastic response of the three different networks in their equilibrium swollen states. Within the measured frequency regime, both 9<sub>80/20D</sub> and 10<sub>80/20</sub> exhibit no frequency dependence as would be expected for covalent networks. However, 8<sub>80/20D</sub> showed two plateaus in the storage moduli ( $E'$ ), one at high frequencies ( $\omega > 100 \text{ rad s}^{-1}$ ) and a second at low frequencies ( $\omega < 1 \text{ rad s}^{-1}$ ). At the higher frequencies, the storage modulus of 8<sub>80/20D</sub> is ca. 150 kPa, similar to 9<sub>80/20D</sub> and 10<sub>80/20</sub> (Fig. 6b). However, the plateau storage modulus of 8<sub>80/20D</sub> at low frequency ( $\omega < 1 \text{ rad s}^{-1}$ ) decreases to 45 kPa. A peak is observed in the loss factor ( $\tan \delta$ ) at a frequency ( $\omega = 3 \text{ rad s}^{-1}$ ) consistent with this transition in  $E'$  for 8<sub>80/20D</sub> and is absent from 9<sub>80/20D</sub> and 10<sub>80/20</sub> (Fig. 6b). This transition is consistent with the sliding transition that has been observed before by Ito and co-workers in other classes of SRNs.<sup>65–68</sup> The data is consistent with the SR crosslinks behaving akin to fixed crosslinks at high frequencies, while at low frequencies, the polymers have the time to slide through rings, resulting in a softer material. The frequency sweep of the other SR-PCNs in the series also shows a frequency-dependent transition that leads to a lower plateau storage modulus at low frequency and a relaxation peak in  $\tan \delta$  (Fig. S76 and S77). No such transition was observed in any of the control networks 9<sub>a/bD</sub> and 10<sub>a/b</sub> (Fig. S78 and S79).

Uniaxial tensile tests were conducted to further probe the mechanical properties of these gels. Gel 8<sub>80/20D</sub> exhibited lower true stress ( $\sigma_{\text{true}}$ , calculated from the equation  $\sigma_{\text{true}} = \sigma_{\text{eng}} \times (1 + \varepsilon_{\text{eng}})$  where  $\sigma_{\text{eng}}$  and  $\varepsilon_{\text{eng}}$  are engineering stress and strain, respectively) across the measured elongation ratio range ( $\lambda = 1–3$ ) than 9<sub>80/20D</sub> and 10<sub>80/20</sub> with the same percentage of the different crosslinks (Fig. 6c). Of course, the tensile properties of the gels are also related to their  $Q$ , with the more swollen gels yielding softer networks. However, after normalizing the effect of  $Q$  by  $\sigma_{\text{true}} \cdot Q$  and  $\lambda \cdot Q^{1/3}$ ,<sup>69</sup> 8<sub>80/20D</sub> was still a softer network than either 9<sub>80/20D</sub> or 10<sub>80/20</sub> (Fig. 6c). The other 8<sub>a/bD</sub> series also showed lower true stress than the corresponding control gels (Fig. S80 and S81), highlighting the impact of the dtSRs in the network.

To better understand the mechanisms underlying the properties of the differently crosslinked networks, molecular dynamics simulations of a coarse-grained model of the

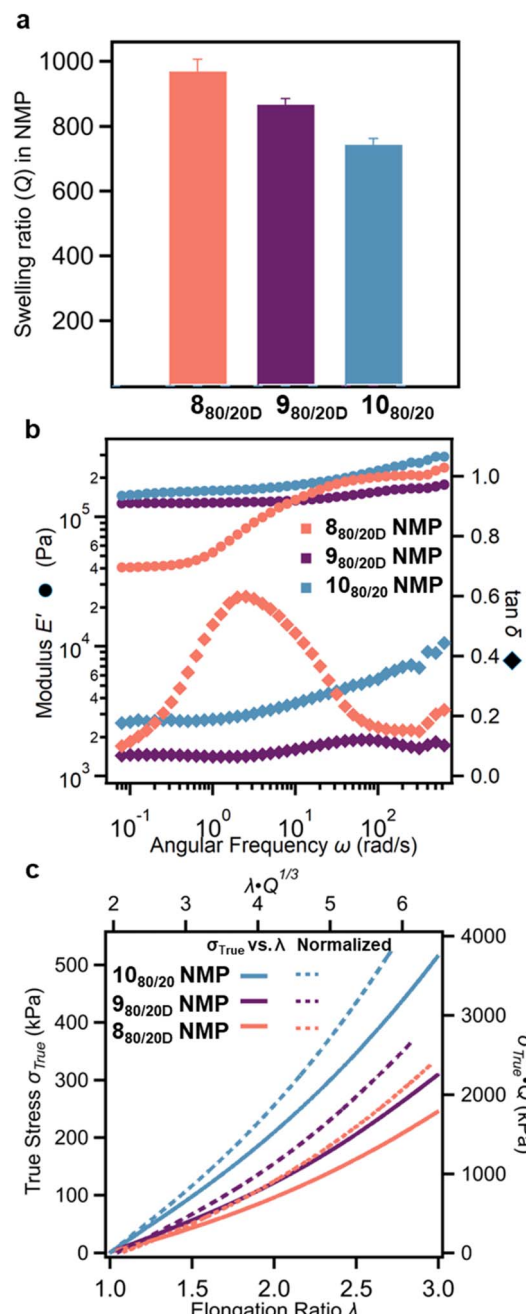


Fig. 6 (a) Swelling ratio ( $Q$ ) of SR-PCN 8<sub>80/20D</sub>, 9<sub>80/20D</sub>, and 10<sub>80/20D</sub> in NMP. (b) Storage moduli  $E'$  and loss factor  $\tan \delta$  of 8<sub>80/20D</sub>, 9<sub>80/20D</sub>, and 10<sub>80/20D</sub> in NMP by SAOC. (c) True stress-elongation ratio curves of swollen 8<sub>80/20D</sub>, 9<sub>80/20D</sub>, and 10<sub>80/20D</sub> in NMP (solid lines). The elongation ratio,  $\lambda$ , is defined as the ratio of the extended length,  $L$ , to its original length,  $L_0$ , given by  $\lambda = L/L_0$  (strain rate of  $20\% \text{ min}^{-1}$  with  $\lambda$  limited to 3, before the material breaks). Dotted lines show after normalizing by the swelling ratio ( $\sigma_{\text{true}} \cdot Q$  and  $\lambda \cdot Q^{1/3}$ ).

networks were performed under swollen conditions (Fig. 7a). The models consist of spherical interaction sites connected by springs and include covalent crosslinks and rings. More specifically, both the dtSR-PCN and the tangled network have 20% of the covalent crosslinks replaced with dtSRs and entangled-like structures, respectively. These network



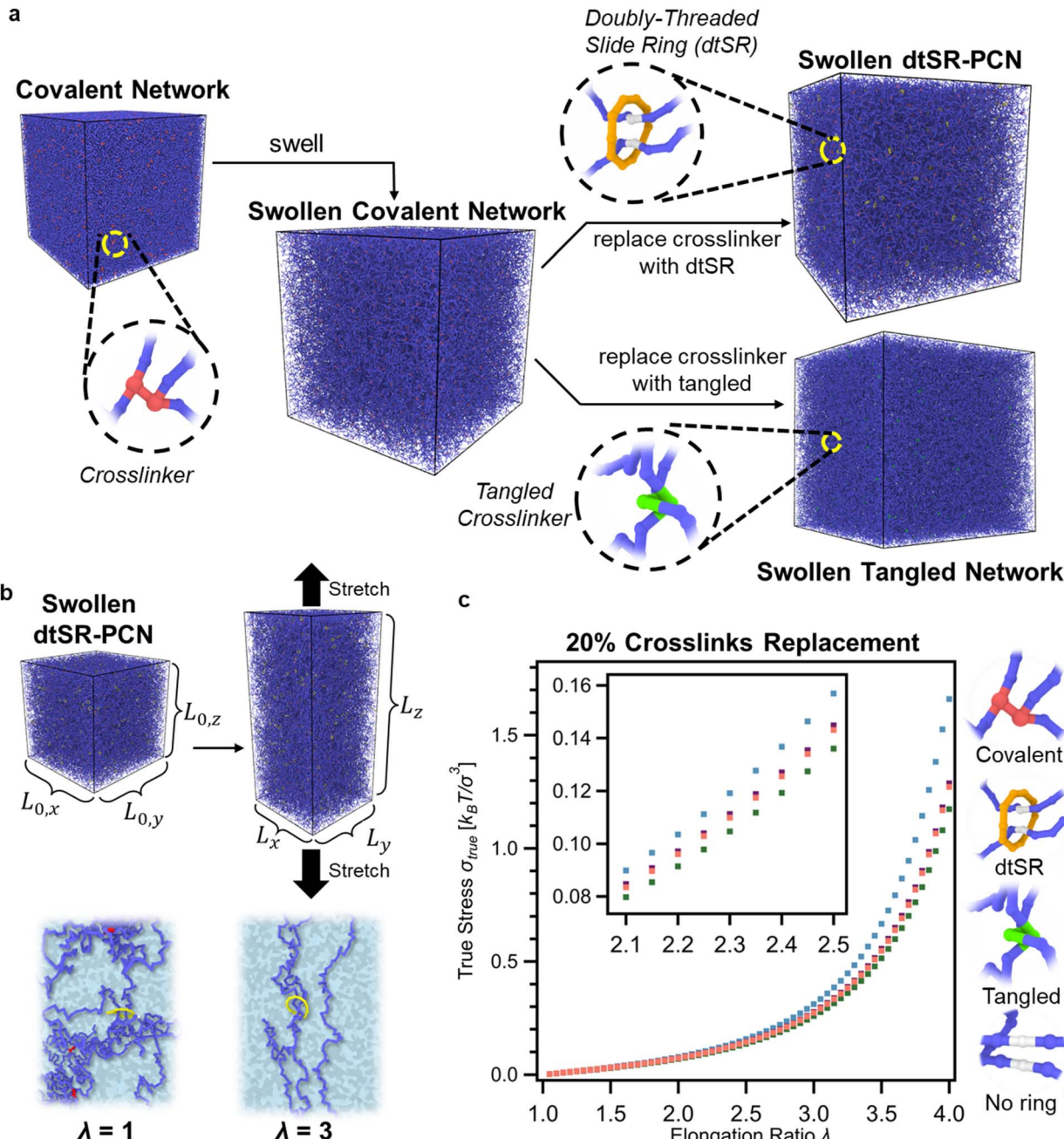


Fig. 7 (a) Snapshots from coarse-grained molecular dynamics simulations illustrating polymer networks with different crosslinking architectures. The covalent polymer network is randomly crosslinked by precursor chains (blue) with a degree of polymerization of 1025 and with network strands composed of an average of 150 bonds between crosslinking bonds (red). The doubly threaded SR-PCN replaces conventional crosslinking bonds with doubly threaded slide rings (SRs, yellow). The tangled polymer network incorporates entanglement-like structures (green) as the crosslinking substitutes. In addition to these networks, another network was modeled, which maintains the same topology as the SR-PCN but lacks actual ring crosslinks at the potential crosslinking points (white), resulting in a network (termed no-ring network) with effectively lower crosslink density. (b) Illustration of uniaxial deformation of swollen SR-PCN, accompanied by snapshots of the SR-PCN structures in the undeformed ( $\lambda = 1$ ) and stretched ( $\lambda = 3$ ) states. (c) True stress-elongation curves obtained by the computer simulation of the polymer networks with different crosslinking architectures: covalent network (blue), SR-PCN (coral), tangled network (purple), and no-ring network (olive). The insert shows a magnified view of the dependence of true stress on elongation ratio in the range of  $\lambda = 2.1$  and 2.5.

configurations are derived from the randomly crosslinked covalent networks with linear strands, each comprising 150 bonds between crosslinking points, denoted as  $n_x = 150$ , thereby preserving similar topologies across the different

network types (Fig. 7a and S82).<sup>70</sup> Upon deformation, the evolution of the dtSR and its two associated network strand conformations revealed that the SRs situated on the network strands aligned with the deformation direction exhibited larger

displacements relative to those oriented otherwise, indicating enhanced mobility of those rings under tensile stress (Fig. 7b and S83). Furthermore, stress-elongation curves from deformation simulations of the different crosslinked networks show that the covalent network exhibits the highest stress compared to both the SR-PCN and tangled networks. Notably, the tangled network demonstrates slightly higher stress than the SR-PCN as a result of reduced flexibility inherent in its entangled-like structures. These findings are in good agreement with the experimental true stress-elongation behavior (Fig. 7c).<sup>71</sup> Finally, by removing the same fraction and locations of crosslinking bonds from the covalent networks, mirroring the replacements made in the SR-PCN and tangled networks, a network akin to the SR-PCN but lacking rings was constructed. This no-ring network has a reduced crosslink density with longer strands between the crosslinks, which results in a softer gel.<sup>69,70</sup> With a better understanding of how different network architectures impact the gel properties, the next step was to explore the effect the amount of SR crosslinks has on these properties. In the SR-PCN **8<sub>a/bD</sub>** series, replacing the covalent crosslinks with SR crosslinks results in an increase in  $Q$  to a greater degree than that of corresponding tangled gels **9<sub>a/bD</sub>** despite the same BIP-PEG polymer backbone for **8<sub>a/bD</sub>** and **9<sub>a/bD</sub>** (Fig. S74). From the SAOC frequency sweep of the SR-PCN series, the value of  $E'$  at both high-frequency and low-frequency ranges decreases (Fig. 8a) when more SR crosslinks replace the covalent crosslinks, consistent with a larger mesh size. This contrasts with the covalent series (**10<sub>a/b</sub>**), where  $E'$  increases as more of the lower molecular weight **4<sub>5k</sub>** crosslinking units are added as they reduce the molecular weight between crosslinks and therefore the mesh size (Fig. S84). Interestingly, in the SR-PCNs, the frequency for the sliding transition exhibits a strong dependence on the number of SR crosslinks in the series of **8<sub>a/bD</sub>**. With an increasing number of rings, the sliding transition (peak in  $\tan \delta$ ) shifts to lower frequencies (Fig. 8a). This observation would be consistent with a larger mesh size with more SR crosslinks, leading to a longer characteristic length scale.

With an interest in probing these interlocked networks over a broad range of time scales, dynamic light scattering (DLS) microrheology<sup>72–74</sup> was used to explore the viscoelastic behavior of **8<sub>a/bD</sub>** across time scales ( $\omega \leq 500\,000 \text{ rad s}^{-1}$ ) beyond traditional rheological experiments ( $\omega \leq 1000 \text{ rad s}^{-1}$ ). This was achieved by adding trimethylsilyl-functionalized silica particles ( $D = 500 \text{ nm}$ ) during the syntheses of these networks (see SI for details). At low to intermediate frequencies ( $\omega \leq 1000 \text{ rad s}^{-1}$ , longer time scale) in the DLS microrheology, the SR-PCNs showed a plateau storage shear modulus  $G'$  with a weak frequency dependence on account of the polymers constrained by the matrix. At these time scales **8<sub>a/bD</sub>**, **9<sub>a/bD</sub>**, and **10<sub>a/b</sub>** (Fig. 8b and S85–S89) showed similar trends in storage modulus between DLS and SAOC rheology. At short time scales ( $\omega \geq 1000 \text{ rad s}^{-1}$ ), DLS microrheology shows that the  $G'$  increases with frequency and the particles probe faster relaxation modes of the rings and subsections of the polymers in these networks. The SR-PCNs with fewer ring crosslinks (**8<sub>90/10D</sub>** and **8<sub>80/20D</sub>**) exhibit characteristic Rouse-model ( $G^* \sim \omega^{1/2}$ ) scaling behavior suggesting that the polymer chains in these networks behave more

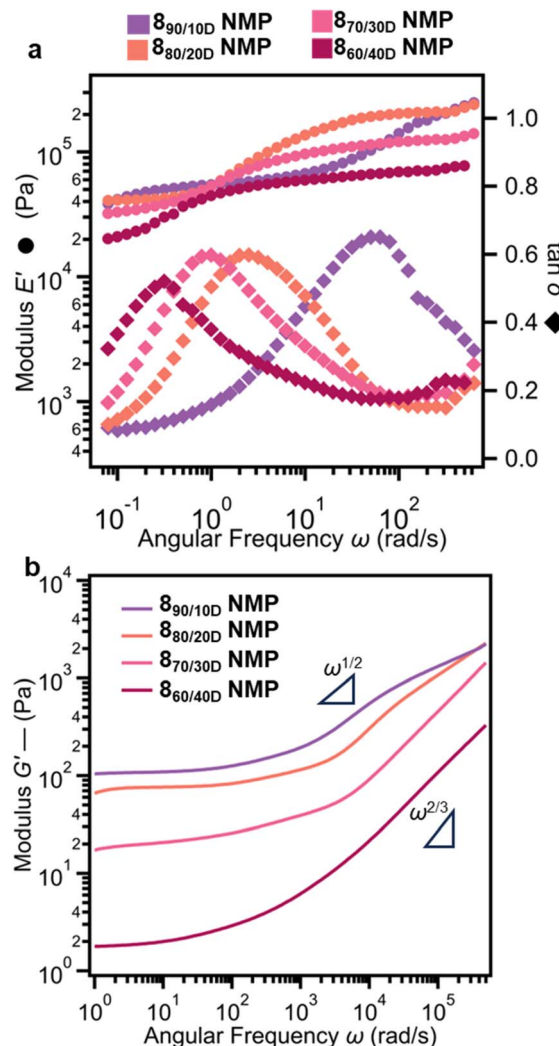


Fig. 8 Effect on viscoelastic properties of the SR-PCNs **8<sub>a/bD</sub>** with varying percentages of SR crosslinks. (a) Compression storage moduli  $E'$  and loss factor  $\tan \delta$  of **8<sub>a/bD</sub>** in *N*-methyl-2-pyrrolidone (NMP) by SAOC. (b) Shear storage moduli  $G'$  of **8<sub>a/bD</sub>** in NMP by dynamic light scattering shear rheology.

akin to concentrated polymer solutions.<sup>72,74</sup> In contrast, the SR-PCNs with higher ring crosslinks (**8<sub>70/30D</sub>** and **8<sub>60/40D</sub>**) show Zimm-model scaling ( $G^* \sim \omega^{2/3}$ ), which is generally what is observed in dilute or semidilute polymer solutions.<sup>75</sup>

Tensile testing of **8<sub>a/bD</sub>**, conducted through both simulations and experiments (Fig. 9a and b), indicates a decrease in true stress with elongation when introducing more rings (e.g. **8<sub>90/10D</sub>** and **8<sub>60/40D</sub>** have a true stress of 298 kPa and 104 kPa, respectively, at an elongation ratio of 3). Moreover, Young's modulus ( $E$ , Fig. S90) from experiments shows a decrease (from *ca.* 94 kPa for **8<sub>90/10D</sub>** to *ca.* 34 kPa for **8<sub>60/40D</sub>**) when the SR-PCNs contain more ring crosslinks. These observations which can be explained, at least in part, with increased swelling of the SR-PCNs with more ring crosslinks. Comparison of stress-elongation curves between simulations (dotted lines in Fig. 9b) and experiments (solid lines in Fig. 9b) provides deeper insights into how the addition of the P3R crosslinker into the

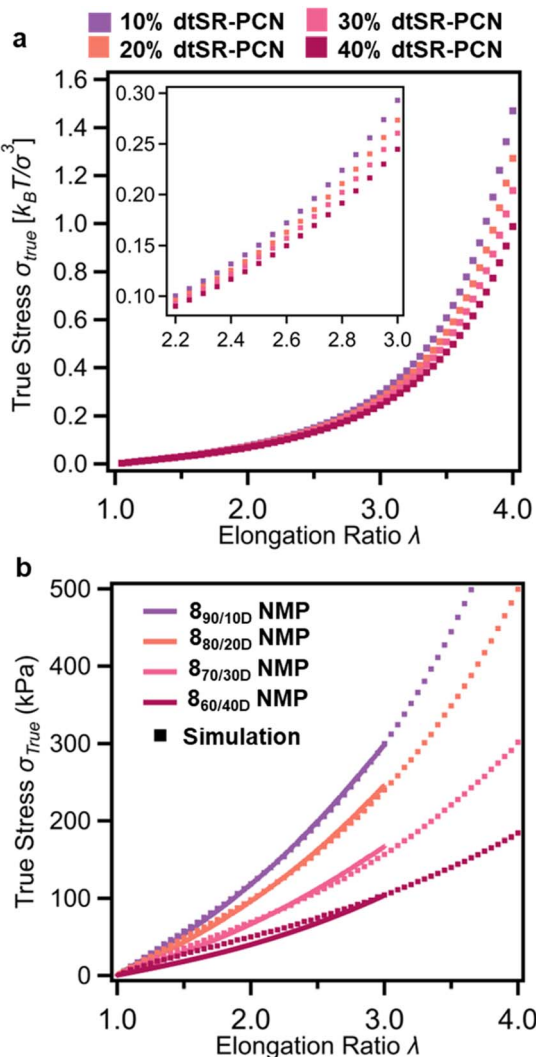


Fig. 9 Tensile properties of the SR-PCNs  $8_{a/bD}$  with different percentages of SR crosslinks and simulation studies on the SR-PCN swollen in NMP. (a) Dependence of the true stress  $\sigma_{true}$  on elongation ratio  $\lambda$  obtained in simulations of dtSR-PCN made by crosslinking precursor chains with the degree of polymerization of 1025 and  $n_x = 150$ . (b) True stress-elongation ratio curves of the SR-PCNs  $8_{a/bD}$  by experimental tensile testing (solid lines; strain rate of  $20\text{ min}^{-1}$  with  $\lambda$  limited to 3, before the material breaks) matched with compressive true stress-elongation curves from simulated modified SR-PCN made by crosslinking precursor chains with the degree of polymerization of 1025 and  $n_x = 150$  with defects.

network synthesis alters the network topology and subsequently the mechanical properties. Incorporating swelling effects into the simulations performed at a constant pressure, the stress-elongation behavior of the dtSR-PCN model with a 10% ring fraction closely matches experimental results (Fig. S91). However, discrepancies between experimental and simulated stress-elongation behaviors were observed for dtSR-PCNs with ring fractions ranging from 20% to 40%. To address these inconsistencies, the impact of network defects was explicitly considered. For example, reducing the functionality ( $f$ ) of 12.5% of the total covalent crosslinks from 4 to 3 in the 20% dtSR-PCN

model resulted in a match to the experimental data of  $8_{80/20D}$  (Fig. S91). To achieve a comparable match with the experimental results of  $8_{70/30D}$ , the 30% dtSR-PCN model required conversion of 20% of the covalent crosslinks ( $f = 4$ ) to  $f = 2$  (Fig. S91). It should be noted that, in both cases, no covalent crosslinks adjacent to the SR crosslinks were altered. Both of these results suggest that the addition of the P3R crosslinker in the synthesis does increase the defects in the gels. For the 40% dtSR-PCN model to match with the experimental  $8_{60/40D}$  true stress-elongation data, more significant addition of network defects was required. In addition to reducing 15% of the covalent crosslinks to  $f = 2$ , akin to what was done before, it was necessary to randomly remove 20% of the total covalent crosslinks in the network, as shown in Fig. S91 (see SI for details). It is important to note that while the experimental SR-PCNs may not have an identical topology as the simulated dtSR networks, these results do demonstrate that addition of more P3Rs in the synthesis results in increased network defects. This increase in defects can be explained, at least in part, by the observed increase in the formation of catenane byproducts when using more P3Rs in the synthesis (Fig. 3b and S92). No matter the cause of the defects it is important to note that the resulting topological changes will certainly contribute to the observed decrease in the network stiffness.

To better explore the impact of solvent on these SR-PCNs,  $8_{80/20D}$  was swollen in propylene carbonate (PC), dimethyl sulfoxide (DMSO), and water. The  $Q$  in these different solvents is shown in Fig. 10a, with  $8_{80/20D}$  exhibiting the highest swelling in NMP (ca. 970%), followed by PC (ca. 870%) and DMSO (ca. 740%).  $8_{80/20D}$  gels appear optically transparent in these solvents and possess a strong blue fluorescence under 365 nm UV light, consistent with the free BIP ligand (Fig. 10b and S93).<sup>76</sup> SAOC of the organogels of  $8_{80/20D}$  (Fig. 10c and S94) show that they all exhibit the sliding transition; however, the frequency of the  $\tan \delta$  peak varies depending on the solvent. As mentioned above in NMP, the peak in  $\tan \delta$  is observed at a frequency of  $3\text{ rad s}^{-1}$ . The peak moves to higher frequencies in PC ( $80\text{ rad s}^{-1}$ ) and DMSO ( $500\text{ rad s}^{-1}$ ) gels. This peak in  $\tan \delta$  tracks with the  $Q$  in the organogels, suggesting that this could be attributed to variations in the degree of polymer chain stretching in the gel networks. For example, the  $8_{80/20D}$  gels with a smaller  $Q$  suggest that the polymer chains are less stretched, and the sliding of the ring occurs at higher frequencies on account of a shorter ring sliding path.

In water,  $8_{80/20D}$  shows reduced swelling (ca. 530%) and exhibits a weakly fluorescent blue color under 365 nm UV light (Fig. 10b). The fluorescence spectrum of the  $8_{80/20D}$  hydrogel shows a broader, lower-intensity emission peak relative to the peak in NMP. Furthermore, there is a bathochromic shift in the emission peak from 439 nm for  $8_{80/20D}$  in NMP to 484 nm for the  $8_{80/20D}$  hydrogel (Fig. S95). This observation is consistent with the stacking/aggregation observed for other fluorophores.<sup>64,77-79</sup> Taken together, the swelling and fluorescence data support the aggregation of the BIP moieties in the hydrogels. Furthermore, the SAOC of the aqueous gel shows no sliding transition and a disappearance of the characteristic  $\tan \delta$  peak in the frequency sweep (Fig. 10c and S94) and its  $E'$  storage modulus is similar to



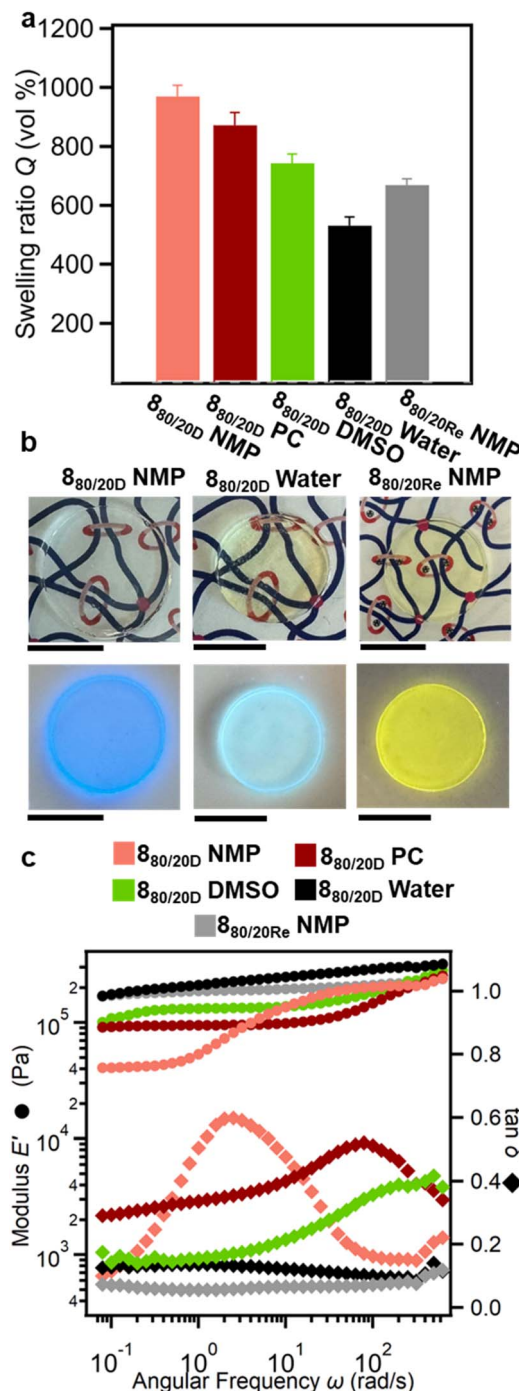


Fig. 10 Swelling behavior and viscoelastic properties of SR-PCN swollen with different solvent and with metalation. (a) Swelling ratios of demetalated SR-PCN  $8_{80/20D}$  in NMP, propylene carbonate (PC), dimethyl sulfoxide (DMSO), and water and the remetalated SR-PCN  $8_{80/20Re}$  in NMP. (b) Optical images of  $8_{80/20D}$  swollen in NMP and water and  $8_{80/20Re}$  swollen in NMP under ambient light (top) and under 365 nm UV light (bottom). 1 cm scale bar (c) storage moduli  $E'$  and loss factor  $\tan \delta$  of the demetalated SR-PCN  $8_{80/20D}$  in different solvents and after remetalation.

that of the covalent gel. Thus, while the PEG backbone is soluble in water, the BIP moieties used in the ring and backbone of the  $8_{80/20D}$  are not, which hinders ring mobility and prevents sliding.

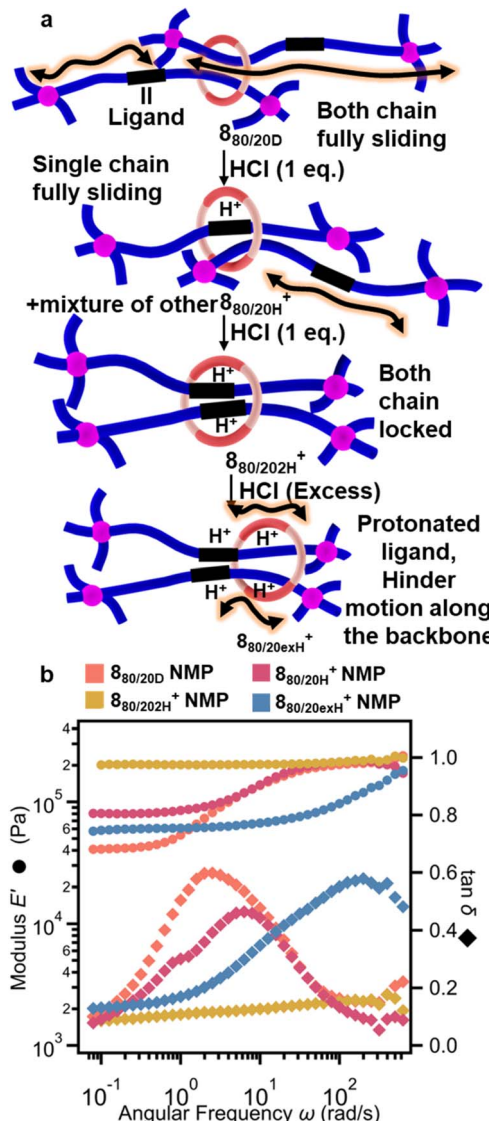


Fig. 11 (a) Schematic showing the proposed impact of the addition of acid to the SR-PCN. The unprotonated  $8_{80/20D}$  allows polymer/ring mobility. Partial protonation with one equivalent of acid ( $8_{80/20H^+}$ ) binds some of the polymer chains and the rings. Addition of two equivalents of acid ( $8_{80/202H^+}$ ) results in the formation of interlocked  $BIP_2:H^+$  complexes that locks the ring and polymer (no sliding). Further protonation on the BIP moieties ( $8_{80/20exH^+}$ ) results in reengaging the ring and polymer mobility on account of electrostatic repulsion. (b) Storage moduli  $E'$  and  $\tan \delta$  of SR-PCN  $8_{80/20D}$  in NMP with different amounts of added acid.

To further explore the impact of the ring mobility within the SR-PCN gels, the responsiveness of the gels to the addition of metal ions or acid was also examined. Given that these SR-PCNs contain ligands, an obvious method to inhibit ring mobility is to explore the remetalation of the gels. Upon adding enough  $Zn(NTf_2)_2$  to the network to obtain 1 : 2 metal-ligand complexes, the  $8_{80/20Re}$  NMP gel exhibits a pale-yellow color and fluoresces yellow under 365 nm UV light (Fig. 10b), both consistent with the formation of  $Zn(II):BIP_2$  complexes.<sup>76</sup> The remetalated  $8_{80/20Re}$  exhibited reduced swelling in NMP (ca. 670% vs. 970% for

**8<sub>80/20D</sub>**), consistent with the presence of additional crosslinks. Furthermore, SAOC showed only one plateau in  $E'$  and no peak in  $\tan \delta$  in the frequency sweep (Fig. 10c), akin to what is observed in the fully covalent networks. This is consistent with remetalation locking the rings in place.

The BIP ligands in these SR-PCNs can also be protonated, so it was of interest to see if the behavior of these gels was sensitive to the addition of acid. In 1986, Sauvage reported that phenanthroline-based [2]catenanes exhibit enhanced basicity, and protonation results in the formation of interlocked phenanthroline<sub>2</sub>:H<sup>+</sup> complexes that switch off the relative component motions,<sup>80</sup> making them a class of pH-sensitive MIMs.<sup>81,82</sup> As such, it was hypothesized that the presence of the interlocked, basic BIP moieties should result in acid-responsive SR-PCNs. To investigate this, SAOC was used to measure the viscoelastic properties of the SR-PCNs with varying amounts of acid (Fig. 11a and S96). Addition of one equivalent of hydrochloric acid with respect to the SR moiety (0.25 equivalent with respect to BIP units) in **8<sub>80/20D</sub>** yields **8<sub>80/20D</sub>H<sup>+</sup>**. A frequency sweep of this gel (Fig. 11b) shows a slight decrease in the intensity of the  $\tan \delta$  peak, which also shifts to slightly higher frequencies. This data is consistent with the protonation of some of the BIP moieties on the ring and thread, resulting in formation of a BIP<sub>2</sub>:H<sup>+</sup> complex that inhibits sliding of the ring (Fig. 11a). The addition of two equivalents of protons with respect to the SR moieties yields the gel **8<sub>80/202H</sub>H<sup>+</sup>** which not only exhibits an  $E'$  similar to that of the covalent or metalated gels, but the frequency sweep data shows no transition in  $E'$  and no peak in  $\tan \delta$ . This data suggests that the rings are no longer mobile and is consistent with the conversion of most of the BIP ligands to BIP<sub>2</sub>:H<sup>+</sup> complexes. Addition of excess acid results in **8<sub>80/20exH</sub>H<sup>+</sup>** exhibiting a reappearance of the transition in  $E'$  and peak in  $\tan \delta$ , albeit at much higher frequencies than **8<sub>80/20D</sub>**. This can be explained by excess protonation of the BIP moieties on both the polymer and rings, leading to electrostatic repulsion of the protonated BIP moieties re-engaging the mobility of the rings (Fig. 11a). The shift in  $\tan \delta$  towards higher frequency is consistent with a shorter ring sliding path length on account of electrostatic repulsions reducing ring movement along the polymer backbone.

## Conclusions

Through the careful design of the relevant components, it has been possible to increase the reaction kinetics of the metal-templated dtP3R crosslinker, allowing it to be more efficiently incorporated into the networks, resulting in SR-PCNs with a significant improvement in gel fraction and ring content. In addition, the use of extended thread components in the P3R and nitrile oxide chain extenders was shown to reduce the amount of catenane byproducts in the network. The improved synthesis of these SR-PCNs, combined with studies on covalent and tangled control networks, has allowed for a much-improved understanding of the impact of the doubly threaded SR crosslinks in these SR-PCNs. Swelling studies, compression rheology, tensile testing, dynamic light scattering microrheology, and molecular modeling were all carried out to compare the

properties of the SR-PCNs with corresponding tangled and covalent networks. While the incorporation of the SRs into the gel results in a higher swelling ratio, the SRs also impart a distinct frequency-dependent mechanical behavior to the gels. At higher frequencies, the SR-PCNs have a compression storage modulus comparable to that of the covalent networks. However, when probed at lower frequencies, gels show a much lower modulus, consistent with movement of the chains through the ring over longer time scales. Supporting these findings, computational simulations revealed that purely covalent networks exhibit the highest stress response, followed by the tangled networks and then the dtSR-PCNs, reflecting the impact of crosslink flexibility and network topology. Further analysis of dtSR-PCN indicated that the introduction of higher amounts of P3R crosslinker in the synthesis introduces more network defects and topological changes, thereby further reducing the stiffness of the networks.

In addition, these SR-PCNs were shown to be stimuli-responsive. Changes in solvent, metalation, and protonation can be used to manipulate the ring sliding, which in turn changes their viscoelastic behavior, particularly the frequency dependence of the gels. Overall, these insights establish a framework for the rational design of dtSR-PCNs with tunable mechanical properties, highlighting the critical importance of having both flexible crosslinks and controlling defects in network structure. The findings of these concerted experimental and computational studies presented in this work have led to a better understanding of how the SR and polymer architecture impact the properties of this class of stimuli-responsive MIPs.

## Author contributions

G. L. and S. J. R. proposed the study. G. L. and J. O. conducted the synthesis, characterization, and analysis of all materials described with the assistance of J. E. H., B. W. R., N. N., and C. A. L. Simulations were conducted by Y. T., H. L., and J. J. d. P. The study was supervised by S. J. R. and J. J. d. P. The manuscript was written by G. L., J. O., Y. T., J. E. H., and S. J. R. The manuscript was written with the contributions from all authors. All authors have given approval to the final version of the manuscript.

## Conflicts of interest

There are no conflicts to declare.

## Data availability

The authors declare that all data supporting the findings of this study, including synthesis and characterization of monomers, supramolecular crosslinkers, and gels, are available within the article and SI.

Supplementary information: synthetic procedures, NMR spectra, fluorescence spectroscopy, swelling and viscoelastic experiments, tensile testing, dynamic light scattering,



molecular dynamics simulations, and additional supporting figures and references. See DOI: <https://doi.org/10.1039/d5sc05459a>.

## Acknowledgements

This work was primarily funded by National Science Foundation (NSF) grant number CHE-2304633 and received additional support from Defense Advanced Research Projects Agency (DARPA) under contract HR00112320039. This work made use of the shared facilities at the University of Chicago Materials Research Science and Engineering Center (MRSEC), supported by National Science Foundation (NSF) under award number DMR-2011854. Parts of this work were carried out at the Soft Matter Characterization Facility (SMCF) of the University of Chicago. We would also like to thank the director of the SMCF, Dr Philip Griffin, for his assistance with mechanical property characterization. We would like to thank the University of Chicago Chemistry NMR Facility and the facility manager Dr Josh Kurutz for helpful discussion on NMR analysis. We would like to thank the University of Chicago Chemistry Mass Spectrometry Facility and the facility manager Dr C. Jin Qin, for his assistance. We would like to thank Dr Pamela C. Cai for helpful discussions on DLS microrheology measurements and Alex E. Crolais for assisting on reaction kinetics calculation.

## Notes and references

- 1 C. J. Bruns and J. F. Stoddart, *The nature of the mechanical bond: from molecules to machines*, John Wiley & Sons, NJ, 2016.
- 2 G. Barin, R. S. Forgan and J. F. Stoddart, *Proc. R. Soc. A*, 2012, **468**, 2849–2880.
- 3 C. J. Bruns and J. F. Stoddart, in *Beauty in Chemistry: Artistry in the Creation of New Molecules*, ed. L. Fabbrizzi, Springer Berlin Heidelberg, Berlin, Heidelberg, 2012, pp. 19–72.
- 4 J. F. Stoddart, *Angew. Chem., Int. Ed.*, 2017, **56**, 11094–11125.
- 5 J. F. Stoddart, *Chem. Soc. Rev.*, 2009, **38**, 1802–1820.
- 6 D. Sluysmans and J. F. Stoddart, *Trends Chem.*, 2019, **1**, 185–197.
- 7 G. Gil-Ramirez, D. A. Leigh and A. J. Stephens, *Angew. Chem., Int. Ed.*, 2015, **54**, 6110–6150.
- 8 Q. Chen and K. Zhu, *Chem. Soc. Rev.*, 2024, **53**, 5677–5703.
- 9 E. R. Kay, D. A. Leigh and F. Zerbetto, *Angew. Chem., Int. Ed.*, 2007, **46**, 72–191.
- 10 A. Van Quaethem, P. Lussis, D. A. Leigh, A.-S. Duwez and C.-A. Fustin, *Chem. Sci.*, 2014, **5**, 1449–1452.
- 11 R. Bai, Z. Zhang, W. Di, X. Yang, J. Zhao, H. Ouyang, G. Liu, X. Zhang, L. Cheng, Y. Cao, W. Yu and X. Yan, *J. Am. Chem. Soc.*, 2023, **145**, 9011–9020.
- 12 Y. Noda, Y. Hayashi and K. Ito, *J. Appl. Polym. Sci.*, 2014, **131**, 40509.
- 13 G. Liu, P. M. Rauscher, B. W. Rawe, M. M. Tranquilli and S. J. Rowan, *Chem. Soc. Rev.*, 2022, **51**, 4928–4948.
- 14 L. F. Hart, J. E. Hertzog, P. M. Rauscher, B. W. Rawe, M. M. Tranquilli and S. J. Rowan, *Nat. Rev. Mater.*, 2021, **6**, 508–530.
- 15 Z. Niu and H. W. Gibson, *Chem. Rev.*, 2009, **109**, 6024–6046.
- 16 S. Ando and K. Ito, *Macromolecules*, 2025, **58**, 2157–2177.
- 17 Y. Okumura and K. Ito, *Adv. Mater.*, 2001, **13**, 485–487.
- 18 C. Liu, N. Morimoto, L. Jiang, S. Kawahara, T. Noritomi, H. Yokoyama, K. Mayumi and K. Ito, *Science*, 2021, **372**, 1078–1081.
- 19 X. Li, H. Kang, J. Shen, L. Zhang, T. Nishi, K. Ito, C. Zhao and P. Coates, *Polymer*, 2014, **55**, 4313–4323.
- 20 A. Bin Imran, K. Esaki, H. Gotoh, T. Seki, K. Ito, Y. Sakai and Y. Takeoka, *Nat. Commun.*, 2014, **5**, 5124.
- 21 L. Jiang, C. Liu, K. Mayumi, K. Kato, H. Yokoyama and K. Ito, *Chem. Mater.*, 2018, **30**, 5013–5019.
- 22 K. Minato, K. Mayumi, R. Maeda, K. Kato, H. Yokoyama and K. Ito, *Polymer*, 2017, **128**, 386–391.
- 23 K. Kato, A. Hori and K. Ito, *Polymer*, 2018, **147**, 67–73.
- 24 Q. Lin, L. Li, M. Tang, S. Uenuma, J. Samanta, S. Li, X. Jiang, L. Zou, K. Ito and C. Ke, *Chem*, 2021, **7**, 2442–2459.
- 25 Q. Lin, L. Li, M. Tang, X. Hou and C. Ke, *J. Mater. Chem. C*, 2018, **6**, 11956–11960.
- 26 Z. Xu, J. Lu, D. Lu, Y. Li, H. Lei, B. Chen, W. Li, B. Xue, Y. Cao and W. Wang, *Nat. Commun.*, 2024, **15**, 4895.
- 27 K. Kato, Y. Ikeda and K. Ito, *ACS Macro Lett.*, 2019, **8**, 700–704.
- 28 A. Bin Imran, T. Seki, K. Ito and Y. Takeoka, *Macromolecules*, 2010, **43**, 1975–1980.
- 29 J. Araki, T. Kataoka and K. Ito, *Soft Matter*, 2008, **4**, 245–249.
- 30 P. R. McGonigal, *Supramol. Chem.*, 2018, **30**, 782–794.
- 31 L. D. Movsisyan, M. Franz, F. Hampel, A. L. Thompson, R. R. Tykwiński and H. L. Anderson, *J. Am. Chem. Soc.*, 2016, **138**, 1366–1376.
- 32 R. Hayashi, Y. Mutoh, T. Kasama and S. Saito, *J. Org. Chem.*, 2015, **80**, 7536–7546.
- 33 S. Huang, Z. Wang, J. Wu, X. Mai, S. Qin, Y. Zhou, D. Yuan, X. Li, W. Feng and L. Yuan, *Chem. Commun.*, 2024, **60**, 5622–5625.
- 34 M. Tang, D. Zheng, J. Samanta, E. H. R. Tsai, H. Qiu, J. A. Read and C. Ke, *Chem*, 2023, **9**, 3515–3531.
- 35 A. Harada, J. Li and M. Kamachi, *Nature*, 1994, **370**, 126–128.
- 36 T. Kureha, D. Aoki, S. Hiroshige, K. Iijima, D. Aoki, T. Takata and D. Suzuki, *Angew. Chem., Int. Ed.*, 2017, **56**, 15393–15396.
- 37 K. Jang, K. Iijima, Y. Koyama, S. Uchida, S. Asai and T. Takata, *Polymer*, 2017, **128**, 379–385.
- 38 K. Iijima, D. Aoki, H. Otsuka and T. Takata, *Polymer*, 2017, **128**, 392–396.
- 39 W. Qiong, R. P. M. L. Xiaolong, W. R. J. P. J. J. de, H. M. J. A., R. S. J. Q. Wu, P. M. Rauscher, X. L. Lang, R. J. Wojtecki, J. J. de Pablo, M. J. A. Hore and S. J. Rowan, *Science*, 2017, **358**, 1434–1439.
- 40 M. M. Tranquilli, Q. Wu and S. J. Rowan, *Chem. Sci.*, 2021, **12**, 8722–8730.
- 41 M. M. Tranquilli, B. W. Rawe, G. Liu and S. J. Rowan, *Chem. Sci.*, 2023, **14**, 2596–2605.
- 42 M. A. Nosiglia, N. D. Colley, M. K. Danielson, M. S. Palmquist, A. O. Delawder, S. L. Tran, G. H. Harlan and J. C. Barnes, *J. Am. Chem. Soc.*, 2022, **144**, 9990–9996.



43 X. Hao, L. Zhandong, W. Wenbo, L. Peiren, L. Junkai, S. Yu, W. Z. Liang, Z. Wenke and H. Feihe, *CCS Chem.*, 2020, **2**, 513–523.

44 W. Wang and H. Xing, *Polym. Chem.*, 2018, **9**, 2087–2091.

45 H. Xing, Z. Li, Z. L. Wu and F. Huang, *Macromol. Rapid Commun.*, 2018, **39**, 1700361.

46 Z. Zhang, J. Zhao, Z. Guo, H. Zhang, H. Pan, Q. Wu, W. You, W. Yu and X. Yan, *Nat. Commun.*, 2022, **13**, 1393.

47 T. Prakasam, S. K. Sharma, F. Ravaux, F. Benyettou, M. Lusi, V. Sabu, P. Bazin, T. Delclos, R. Jagannathan, J. Whelan, M. El-Roz, M. A. Olson, M. Abdellatif, O. S. Mudra, F. Gándara and A. Trabolsi, *Chem.*, 2025, **11**(2), 102307.

48 M. I. Bardot, C. W. Weyhrich, Z. Shi, M. Traxler, C. L. Stern, J. Cui, D. A. Muller, M. L. Becker and W. R. Dichtel, *Science*, 2025, **387**, 264–269.

49 M. Zhang and G. De Bo, *J. Am. Chem. Soc.*, 2020, **142**, 5029–5033.

50 P. Borst and J. H. J. Hoeijmakers, *Plasmid*, 1979, **2**, 20–40.

51 H. C. Renger and D. R. Wolstenholme, *J. Cell Biol.*, 1972, **54**, 346–364.

52 K. Endo, T. Shiroi, N. Murata, G. Kojima and T. Yamanaka, *Macromolecules*, 2004, **37**, 3143–3150.

53 K. Endo, T. Shiroi and N. Murata, *Polym. J.*, 2005, **37**, 512–516.

54 T. Yamanaka and K. Endo, *Polym. J.*, 2007, **39**, 1360–1364.

55 K. Endo and T. Yamanaka, *Macromolecules*, 2006, **39**, 4038–4043.

56 H. Ishida, A. Kisanuki and K. Endo, *Polym. J.*, 2009, **41**, 110–117.

57 L. F. Hart, W. R. Lenart, J. E. Hertzog, J. Oh, W. R. Turner, J. M. Dennis and S. J. Rowan, *J. Am. Chem. Soc.*, 2023, **145**, 12315–12323.

58 B. M. McKenzie, A. K. Miller, R. J. Wojtecki, J. C. Johnson, K. A. Burke, K. A. Tzeng, P. T. Mather and S. J. Rowan, *Tetrahedron*, 2008, **64**, 8488–8495.

59 J. E. Hertzog, G. Liu, B. W. Rawe, V. J. Maddi, L. F. Hart, J. Oh, N. D. Dolinski and S. J. Rowan, *Org. Biomol. Chem.*, 2023, **21**, 6969–6978.

60 J. E. Hertzog, V. J. Maddi, L. F. Hart, B. W. Rawe, P. M. Rauscher, K. M. Herbert, E. P. Bruckner, J. J. de Pablo and S. J. Rowan, *Chem. Sci.*, 2022, **13**, 5333–5344.

61 J. Oh, G. Liu, H. Kim, J. E. Hertzog, N. Nitta and S. J. Rowan, *Angew. Chem., Int. Ed.*, 2024, **63**, e202411172.

62 R. J. Wojtecki, Q. Wu, J. C. Johnson, D. G. Ray, L. T. J. Korley and S. J. Rowan, *Chem. Sci.*, 2013, **4**, 4440–4448.

63 F.-S. Wang, B. J. Kruse, J. C. Dickenson and A. V. Zhukhovitskiy, *Macromolecules*, 2024, **57**, 4016–4023.

64 E. C. Krist, B. J. Kruse, J. C. Dickenson and A. V. Zhukhovitskiy, *Macromolecules*, 2024, **57**, 7878–7883.

65 K. Ito, *Polym. J.*, 2012, **44**, 38–41.

66 K. Kato and K. Ito, *Soft Matter*, 2011, **7**, 8737–8740.

67 K. Kato, K. Karube, N. Nakamura and K. Ito, *Polym. Chem.*, 2015, **6**, 2241–2248.

68 K. Kato, T. Yasuda and K. Ito, *Macromolecules*, 2013, **46**, 310–316.

69 Z. Wang, Y. Tian and A. V Dobrynin, *Macromolecules*, 2023, **56**, 6543–6551.

70 A. V Dobrynin, Y. Tian, M. Jacobs, E. A. Nikitina, D. A. Ivanov, M. Maw, F. Vashahi and S. S. Sheiko, *Nat. Mater.*, 2023, **22**, 1394–1400.

71 Y. Yasuda, T. Masumoto, K. Mayumi, M. Toda, H. Yokoyama, H. Morita and K. Ito, *ACS Macro Lett.*, 2020, **9**, 1280–1285.

72 P. C. Cai, B. A. Krajina, M. J. Kratochvil, L. Zou, A. Zhu, E. B. Burgener, P. L. Bollyky, C. E. Milla, M. J. Webber, A. J. Spakowitz and S. C. Heilshorn, *Soft Matter*, 2021, **17**, 1929–1939.

73 B. A. Krajina, C. Tropini, A. Zhu, P. DiGiacomo, J. L. Sonnenburg, S. C. Heilshorn, A. J. Spakowitz and A. C. S. Cent, *Science*, 2017, **3**, 1294–1303.

74 E. M. Furst and T. M. Squires, *Microrheology*, Oxford University Press, 2017.

75 M. Doi, S. F. Edwards and S. F. Edwards, *The Theory of Polymer Dynamics*, Clarendon, Oxford, 1988.

76 C. U. Lenora, N. Hu and J. C. Furgal, *ACS Omega*, 2020, **5**, 33017–33027.

77 X. Cao, L. Meng, Z. Li, Y. Mao, H. Lan, L. Chen, Y. Fan and T. Yi, *Langmuir*, 2014, **30**, 11753–11760.

78 S. Ravi, S. Karthikeyan, M. Pannipara, A. G. Al-Sehemi, D. Moon and S. P. Anthony, *Mater. Adv.*, 2025, **6**, 3095–3103.

79 J. Herbich, M. Kijak, A. Zielińska, R. P. Thummel and J. Waluk, *J. Phys. Chem. A*, 2002, **106**, 2158–2163.

80 M. Cesario, C. O. Dietrich, A. Edel, J. Guilhem, J. P. Kintzinger, C. Pascard and J. P. Sauvage, *J. Am. Chem. Soc.*, 1986, **108**, 6250–6254.

81 G. Capocasa, F. Frataloreto, M. Valentini and S. Di Stefano, *Commun. Chem.*, 2024, **7**, 116.

82 H.-Y. Zhou, Y. Han and C.-F. Chen, *Mater. Chem. Front.*, 2020, **4**, 12–28.

